Version TOL/3

EGT2
ENGINEERING TRIPOS PART IIB

Tuesday 29 April 2025 9.30 to 11.10

Module 4G7

CONTROL & COMPUTATION IN LIVING SYSTEMS

*Answer **both** questions in section A. Answer **one** question in section B.*

All questions carry the same number of marks.

*The **approximate** percentage of marks allocated to each part of a question is indicated in the right margin.*

*Write your candidate number **not** your name on the cover sheet.*

STATIONERY REQUIREMENTS
Single-sided script paper

SPECIAL REQUIREMENTS TO BE SUPPLIED FOR THIS EXAM
CUED approved calculator allowed
Attachment 1: Hurkey et al. (2023) paper for Question 3 (8 pages)
Attachment 2: London et al. (2010) paper for Question 4 (6 pages)
Engineering Data Book

10 minutes reading time is allowed for this paper at the start of the exam.

You may not start to read the questions printed on the subsequent pages of this question paper until instructed to do so.

You may not remove any stationery from the Examination Room.

SECTION A

Answer **both** questions.

1 (a) Consider biochemical reactions between species $X_1, X_2, ..., X_i$.

(i) What is meant by an elementary reaction involving X_i? [15%]

(ii) Rate equations of reactions often have terms of the form:

$$\frac{k[X_i]}{K + [X_i]^n},$$

where square parentheses represent concentrations. Explain how such terms arise. [15%]

(b) Suppose two animal species, x, y compete for resources according to the following (dimensionless) dynamics:

$$\dot{x} = x(1 - x - y)$$
$$\dot{y} = y(3 - x - \frac{3}{2}y).$$

(i) Provide an interpretation of the terms in the model, stating any assumptions that are required for the model to be valid. [10%]

(ii) Find and analyse the equilibria of this model, and sketch the (x, y) phase plane. [50%]

(iii) Describe the long term behaviour of the model for valid initial conditions. [10%]

2 (a) Figure 1 shows a micrograph of the density of cyclic AMP in a culture of social amoebae, *Dictyostelium*. Explain the origin of the circular and spiral patterns, and their relevance to the life cycle of this species. [30%]

(b) The phases of two coupled oscillators, θ_1, θ_2 are described by the equations:

$$\dot{\theta}_i = \omega_i + H(\theta_i, \theta_j), \quad i, j \in \{1, 2\}, i \neq j,$$

where $k_i > 0$ and $\theta_i = \theta_i \mod 2\pi$. The coupling function is given by:

$$H(\theta_i, \theta_j) = k_i(|\theta_j - \theta_i| - \pi)^2.$$

(i) For what values of k_1, k_2 will the system synchronise? [40%]

(ii) Identify the type of bifurcation that occurs as either k_1 or k_2 approaches a critical value such that the conditions for synchrony are violated. [10%]

(iii) Without performing calculations, describe the behaviour of the system when $\omega_1 = \omega_2 + \epsilon(t)$, where $\epsilon(t)$ is a small amplitude, zero mean noise process. Provide a sketch of the the phase difference, $\phi = \theta_1 - \theta_2$, to aid your description. [20%]

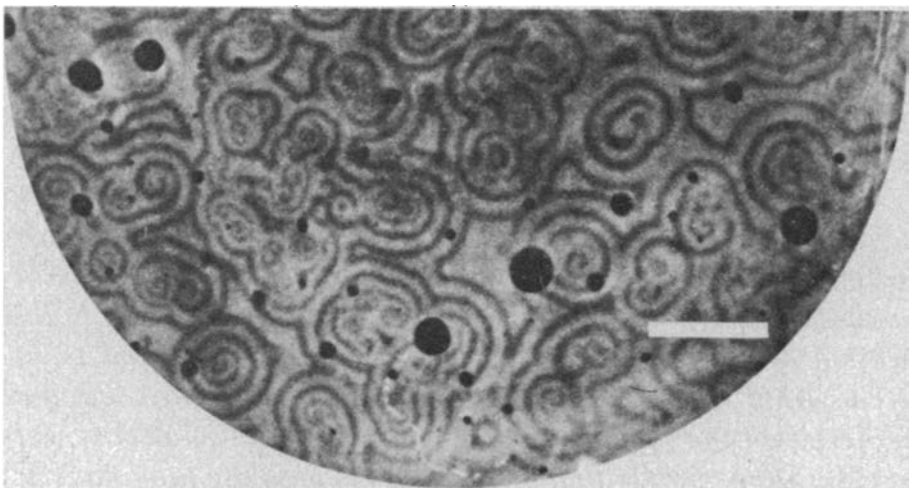

Fig. 1: scale bar = 1cm

SECTION B

Answer **one** question.

3 Refer to the attached paper by Hurkey et al. (2023) Nature.

(a) Summarise the aim, approach, findings and motivation of the paper in no more than 500 words. Provide an interpretation of the results and comment on any limitations of the study. You may use diagrams if you wish. [60%]

(b) Define the phase response curve (PRC) of an oscillator. What is the relevance of a PRC for understanding oscillator dynamics, and under what conditions may it give poor predictions? [40%]

4 Refer to the attached paper by London et al. (2010) Nature.

(a) Summarise the aim, approach, findings and motivation of the paper in no more than 500 words. Provide an interpretation of the results and comment on any limitations of the study. You may use diagrams if you wish. [60%]

(b) What is meant by *rate coding* in the context of London et al's study? Can you envisage biologically plausible alternatives to rate coding? [20%]

(c) Evaluate the logical argument that London et al put forward to argue against rate coding. Is the argument sound? [20%]

END OF PAPER

Article

Gap junctions desynchronize a neural circuit to stabilize insect flight

https://doi.org/10.1038/s41586-023-06099-0

Received: 18 February 2022

Accepted: 18 April 2023

Published online: 24 May 2023

Open access

Check for updates

Silvan Hürkey[1,4], Nelson Niemeyer[2,4], Jan-Hendrik Schleimer[2], Stefanie Ryglewski[1], Susanne Schreiber[2,3,5] ✉ & Carsten Duch[1,5] ✉

Insect asynchronous flight is one of the most prevalent forms of animal locomotion used by more than 600,000 species. Despite profound insights into the motor patterns[1], biomechanics[2,3] and aerodynamics underlying asynchronous flight[4,5], the architecture and function of the central-pattern-generating (CPG) neural network remain unclear. Here, on the basis of an experiment–theory approach including electrophysiology, optophysiology, *Drosophila* genetics and mathematical modelling, we identify a miniaturized circuit solution with unexpected properties. The CPG network consists of motoneurons interconnected by electrical synapses that, in contrast to doctrine, produce network activity splayed out in time instead of synchronized across neurons. Experimental and mathematical evidence support a generic mechanism for network desynchronization that relies on weak electrical synapses and specific excitability dynamics of the coupled neurons. In small networks, electrical synapses can synchronize or desynchronize network activity, depending on the neuron-intrinsic dynamics and ion channel composition. In the asynchronous flight CPG, this mechanism translates unpatterned premotor input into stereotyped neuronal firing with fixed sequences of cell activation that ensure stable wingbeat power and, as we show, is conserved across multiple species. Our findings prove a wider functional versatility of electrical synapses in the dynamic control of neural circuits and highlight the relevance of detecting electrical synapses in connectomics.

With over a million known species, insects comprise the largest group of animals on Earth[6]. Their considerable evolutionary success has been attributed to small body size and the ability to fly. These two features provide access to unutilized niches and rapid translocation, but aerodynamic constraints in small flyers require high wingbeat frequencies, and space constraints demand miniaturization of the central nervous controllers for flight[7]. In 75% of all flying insect species, highly specialized, indirect, asynchronous flight muscles form an oscillatory system that generates wingbeat frequencies of 100–1,000 Hz by reciprocal stretch activation of antagonistic wing muscles to ensure forward propulsion at low Reynolds numbers[1,8]. The flight motoneurons (MNs) that innervate asynchronous flight muscles fire at much lower frequencies, therefore not activating the muscles on a cycle-to-cycle basis. Nonetheless, power output is regulated by a CPG network in the central nervous system that controls MN firing frequencies to adjust the myoplasmic calcium levels that, in turn, regulate wingbeat frequency and amplitude[1]. Although asynchronous flight has emerged independently 7–10 times during evolution[8], neither the principles of CPG architecture for generating MN output from the miniaturized central nervous system of asynchronous flyers nor the functional consequences thereof have been identified.

Asynchronous flight motor patterns

To quantify asynchronous flight patterns and decipher CPG architecture, we used the firing output of the five identified MNs (MN1–5) innervating the dorsal longitudinal wing depressor muscle (DLM) of the genetic model system[9–11] *Drosophila melanogaster* as well as other insect species (to test for generality). The DLM provides the force for wing downstroke, consists of six muscle fibres, each of which is innervated by one of five identified MNs[9–11] (MN1–5; Fig. 1a). MN1–4 each target one of the four most ventral DLM fibres ipsilateral to their somata, whereas MN5 innervates DLM fibres 5 and 6 on the side contralateral to the MN5 soma (Fig. 1a). This neuromuscular architecture is conserved across insect species examined (locust[12], moth[13], blowfly[14]).

In vivo recordings of MN1–5 from their DLM target muscle fibres using simultaneous laser-based wingbeat detection during tethered flight show that each MN fires only every approximately 20th to 40th wingbeat (Fig. 1a–c). Although the firing frequencies of MN1–5 can vary between animals and are adjusted on demand[1,15,16], within a given animal and power demand, all five MNs always fire at the same frequencies (Fig. 1b) and with similar variance in the interspike

[1]Institute of Developmental Biology and Neurobiology (iDN), Johannes Gutenberg-University Mainz, Mainz, Germany. [2]Institute for Theoretical Biology, Humboldt-Universität zu Berlin, Berlin, Germany. [3]Bernstein Center for Computational Neuroscience Berlin, Berlin, Germany. [4]These authors contributed equally: Silvan Hürkey, Nelson Niemeyer. [5]These authors jointly supervised this work: Susanne Schreiber, Carsten Duch. ✉e-mail: s.schreiber@hu-berlin.de; cduch@uni-mainz.de

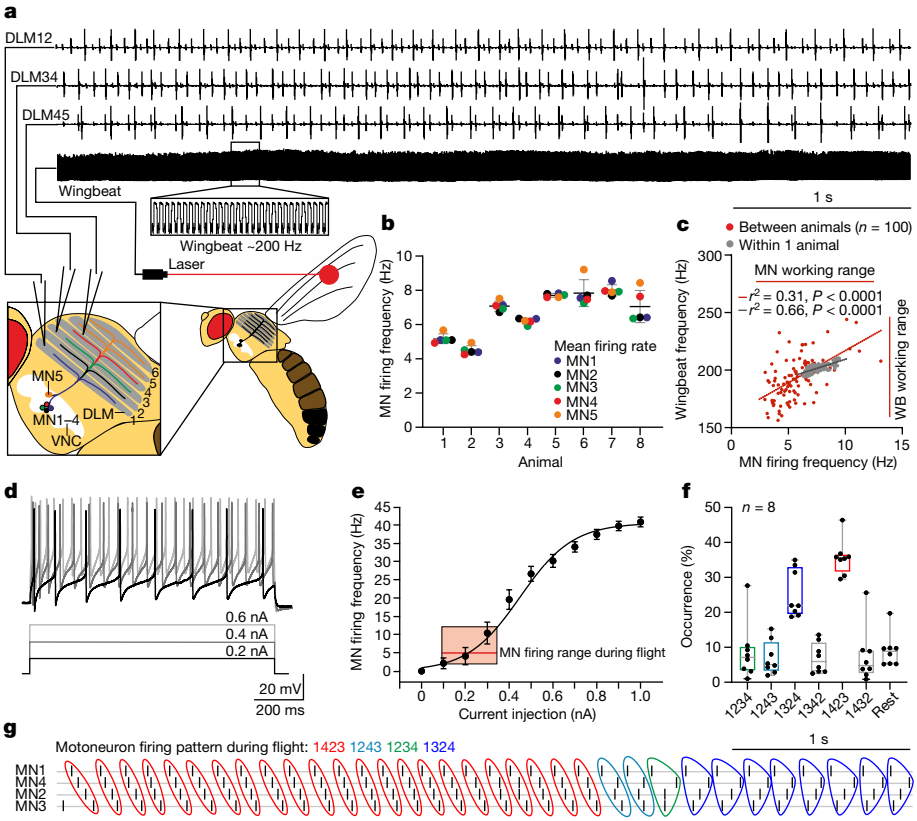

Fig. 1 | Splayed-out MN firing patterns control *Drosophila* flight. **a**, Representative recording of MN1–5 and wingbeat frequency (bottom trace, magnified in the black box) during tethered flight. Colour-coded schematic of MN1–5 in the VNC and axonal projections to the six fibres of the DLM. **b**, Average MN firing frequencies are similar within each animal. The colour code is the same as in **a**. $n = 8$ animals. Data are mean ± s.d. **c**, MN firing frequency and wingbeat (WB) frequency (the red bars indicate working ranges) are linearly related within an animal (grey dots; correlation coefficient, $r^2 = 0.63$; $P < 0.0001$, two-tailed *t*-test) and with larger variance also across animals (red dots; $n = 100$; correlation coefficient, $r^2 = 0.31$; $P < 0.0001$, two-tailed *t*-test). **d**, The firing responses of MNs (top traces) to current injections of different amplitudes (bottom traces). **e**, The mean MN response frequency (f) and injected current amplitude (I) are approximately linearly related for 2–30 Hz ($n = 15$ animals), therefore exceeding the normal MN firing frequencies observed during flight (inset; ~3–12 Hz, data from **c**). Data are mean ± s.e.m. (main plot) and median ± range (inset). **f**, During flight, MN1–4 spikes are dispersed in time (in splay state) with characteristic sequences. Each animal switches between different splay states during flight, but the same splay states are preferred across individuals ($n = 8$). The box plots show the median (centre line), quartiles (box limits) and range (error bars). **g**, Timing of MN1–4 spikes in four subsequent splay states (1423 (red); 1243 (turquoise); 1234 (green); 1324 (dark blue)) during flight.

interval (ISI; coefficient of variation is 0.22 ± 0.07 (mean ± s.d.) for each MN).

MN1–5 firing frequencies directly control muscular tension and stretch activatability by adjusting myoplasmic calcium levels and, therefore, wingbeat frequency and stroke amplitude[1,17]. Accordingly, in single animals, alterations in power demands go along with changes in MN1–5 firing frequency that are proportional to wingbeat frequency changes (Fig. 1c (grey dots)). A linear relationship between average MN firing and average wingbeat frequency within the normal flight working range was further confirmed by recordings in 100 animals, although interanimal variability yields a lower correlation between MN firing rate and wingbeat frequency (Fig. 1c (red dots)). This correlation is increased when analysing the changes in the MN firing rate in relation to changes in the wingbeat frequency (Extended Data Fig. 4e–g). Thus, the central nervous system controls asynchronous flight muscle power output neither by the recruitment of different motor units, nor on the scale of single wingbeats, but the frequency of MN1–5 population firing is the key regulator of wing power production[1]. We show that MN excitability is well suited to dynamically regulate wing power output. First, MN1–5 respond to constant input with slow tonic firing (Fig. 1d). Second, a nearly linear input–output relationship as observed in f–I curves (3–30 Hz; Fig. 1e) covers and even exceeds the working range observed during tethered flight (approximately 3–12 Hz; Fig. 1c). The excitability of MN1–5 is therefore tuned to linearly translate synaptic input into tonic firing to regulate wingbeat in the working range of flight.

Despite equal firing frequencies at any given wingbeat frequency[1,15] (Fig. 1a,b), the five MNs in this system do not fire in synchrony. Instead, as previously suggested[18], their spikes are splayed-out in time with firing phases across neurons dispersed approximately equidistantly, resulting in stereotyped preferred sequences of MN1–5 spiking (Fig. 1g), which we name splay states. A network splay state means that each individual cell in a network of N neurons fires regularly, yet with a constant, non-zero phase relationship with respect to the firing of each other neuron. Firing phase differences between neurons approximately correspond to 1/Nth of a neuron's ISI or a multiple (<N) thereof. Importantly, the sequence of MN1–5 firing can change intermittently, but the CPG robustly slides back into one or two of the most preferred splay states. Notably, the same splay states are preferred across animals (Fig. 1f), indicating that they result from hard-wired CPG circuitry. Splayed-out firing results in characteristic phase relationships between each pair of MN1–5. These phase relationships are conserved across individuals (Extended Data Fig. 1a–c). The phase relationships of all MN1–5 pairs show a gap around phase zero, indicating out-of-phase firing. Given that multiple splay states exist during flight (Fig. 1f,g), firing of MN pairs is not precisely phase locked (Extended Data Fig. 1a–c). Yet, restricting phase histograms to

one splay state narrows the phase relations (Extended Data Fig. 1d). Moreover, synchronous spikes between MN pairs occasionally occur during switches between different splay states, but not within a stable splay state (Extended Data Fig. 1d).

Our characterization of phase relationships between pairwise combinations of the MN1–5 enables us to test for across-species conservation of the motor patterns (see Supplementary Videos 1–3 for the flight of three species). This reveals a notable similarity between *D. melanogaster* and the gold fly *Lucilia* sp. (Extended Data Fig. 2a,b). Similar phase relationships have also been suggested for *Calliphora erythrocephala*[14], *Eucaliphora lilaea* and *Musca domestica*. Moreover, using the MN4–MN5 pair (Extended Data Fig. 2c), our measurements indicate conservation of CPG architecture between two *Drosophila* species (*D. melanogaster* and *Drosophila hydei*), other dipteran genera (*Calliphora* and *Musca*) and, to a certain degree, even between *Diptera* (for example, flies) and *Hymenoptera* (for example, honey bee). Given that asynchronous flight evolved multiple times independently[8], splayed-out firing has probably provided selective benefits over millions of years. To gain mechanistic and functional insights into the CPG network that controls asynchronous flight, we next analysed the network principles underlying splay state motor pattern generation and the resulting functional benefits for flight performance.

Network splay states produced by a minimal CPG

From invertebrates[19] to mammals[20], the timing and pattern of MN activation during locomotion typically rely on networks of premotor interneurons. By contrast, we provide evidence that splayed-out MN1–5 firing is generated by interactions between the MNs themselves. First, unpatterned optogenetic activation of excitatory, cholinergic input to MN1–5 increases MN firing frequencies without changing their phase relationships, preserving a characteristic gap around phase 0 (Extended Data Fig. 3). We confirmed both physiologically[21] and anatomically that MNs receive excitatory cholinergic input to their dendrites (Extended Data Fig. 4a,b), and that all MNs share common synaptic input (Extended Data Fig. 4c,d) as previously proposed[18]. Tonic common excitatory synaptic drive to MN1–5, as induced by optogenetic stimulation, is therefore transformed into out-of-phase MN1–5 firing. Second, unpatterned, tonic, optogenetic stimulation of the five MNs (see Extended Data Fig. 5a,b for selective expression of transgenes in MN1–5) during flight increases their firing frequency and, therefore, wingbeat power, but it does not change phase relationships between MNs, as exemplified by the same characteristic gap around phase 0 for the MN4–MN5 pair (Extended Data Fig. 5). The strength of this dip around phase 0 in MN phase histograms is strongly correlated with full network splayness (definitions are provided in the Methods) in both simulated and experimental data (Extended Data Fig. 6). Similar phase histograms of MN pairs before and during optogenetic stimulation therefore indicate unaltered splayness. The generation of continuous splayed-out firing after selective, unpatterned, optogenetic stimulation of all five MNs indicates that interactions between MNs shape the firing patterns. An alternative possibility would be synaptic output from MN1–5 to feedback interneurons, which then generate the pattern. However, neither trans-synaptic mapping nor genetic markers for central output synapses from MN1–5 provide evidence for postsynaptic partners in the ventral nerve cord (VNC; Extended Data Fig. 7). Thus, it seems probable that the timing and pattern of MN activation does not require patterned activity of interneurons and, instead, the MN1–5 ensemble constitutes a minimal CPG.

One possible mechanism to transform common excitatory input to an ensemble of MNs into dispersed firing is lateral inhibition among MN1–5 by chemical synapses[15]. We reject this possibility by combining targeted genetic manipulation of MNs with in vivo recordings during flight. Knockdown (KD) of receptors for inhibitory transmitter (GABA A receptors (GABA-ARs) and glutamate-gated chloride channel (GluCl)) increases MN firing frequencies, but the phase relationships remain similar (Extended Data Fig. 6e,f). Lateral inhibition through chemical synapses is therefore not required for pattern generation.

Another possibility to create a neural network exclusively from MN1–5 is to connect them with electrical synapses. This has previously been suggested[22,23,24], but experimental evidence has been lacking, and electrical coupling seems difficult to reconcile with desynchronized firing. We have tested this by genetic manipulation of innexins[25], the invertebrate counterparts of connexins[26], which comprise the pore-forming proteins of electrical synapses. ShakingB (ShakB) is the innexin expressed in the *Drosophila* escape circuit, including in MN1–5. KD of *shakB* using RNA interference (RNAi) in MN1–5 reduces electrical coupling below the detection threshold in paired patch-clamp recordings (Fig. 2g).

Genetic manipulation of *shakB* in the five MNs disrupts the splay state without affecting the firing frequencies (Fig. 2a,b). As exemplified for the MN4–MN5 pair, in control animals ($n = 7$), firing of MN5 is inhibited before and after the occurrence of MN4 spikes (Figs. 2a,b (top)), therefore resulting in a characteristic gap around phase 0 (Extended Data Figs. 3b and 5e) that is indicative for network splayness (Extended Data Fig. 6a–d). By contrast, with *shakB* KD in MN1–5, the gap around phase 0 is absent and firing is more random with a slight preference for in-phase firing (Fig. 2a,b (middle)). Thus, electrical synapses are required for firing desynchronization in this small CPG. Recordings of all five MNs during flight confirm that *shakB* KD in MNs impairs their normal phase relationships and, therefore, the splay state (compare Extended Data Fig. 8 with Extended Data Fig. 1). This contradicts the common notion that electrical synapses function to synchronize network activity[27].

Key to this role of gap junctions is weak electrical coupling, because increasing electrical coupling by overexpression of ShakB in MN1–5 causes firing synchronization (Fig. 2a,b (bottom)). Thus, the in vivo data indicate that weak electrical synapses cause firing desynchronization, but stronger coupling synchronizes firing. Weak electrical coupling between MN1–5 is also supported by anatomical experiments. Although we have previously not observed diffusion of small dye tracer molecules through gap junctions between MN1–5[16,21], in *Drosophila* neurons, dye uptake during iontophoresis and subsequent diffusion through *shakB*-encoded electrical synapses are increased by KD of the fragile-X mental retardation protein (FMRP) (encoded by *dfmr1*)[28]. In this genetic background dye coupling of MNs is reliably observed (Fig. 2c).

In summary, a minimal CPG of five electrically coupled MNs is sufficient to pattern splayed-out firing across power demands and does not rely on additional interneurons or chemical synapses. First, lateral inhibition by chemical synapses is not required (Extended Data Fig. 6e,f); second, we found no evidence for chemical output synapses from MN1–5 in the VNC (Extended Data Fig. 7); third, unpatterned optogenetic activation of either presynaptic cholinergic neurons or the MNs during tethered flight increases MN1–5 firing rates and wingbeat frequency (Extended Data Figs. 3 and 5), but the phase relationships between MNs remain unaltered (compare Fig. 2a with Extended Data Figs. 3b and 5e). Finally, weak electrical synapses between MNs are required to generate normal phase relationships (Fig. 2a,b). However, this raises the question of how electrical synapses cause firing desynchronization.

Electrical coupling within the CPG

A first step in deciphering the mechanism is to characterize the electrical synapses. Dual in situ patch-clamp recordings of MN pairs confirm electrical coupling and demonstrate that the electrical synapses are weak, bidirectional and non-rectifying (Fig. 2d). Non-rectifying, because depolarizing and hyperpolarizing current injections (20 ms duration) into one MN cause gap junctional potentials in the other

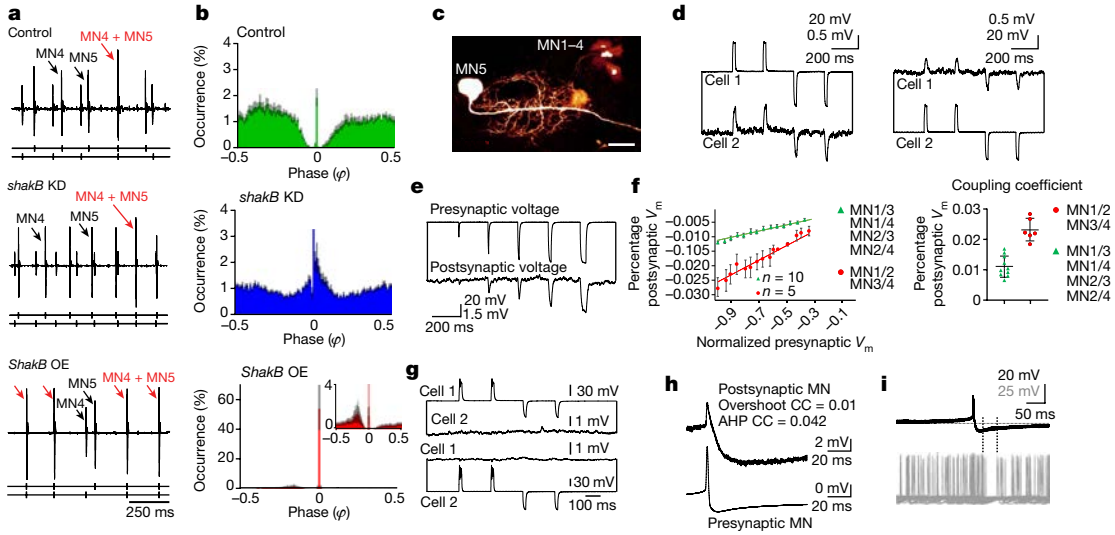

Fig. 2 | Electrical synapses shape CPG output by desynchronizing MN firing. **a**, Representative recording of MN4 and MN5 during tethered flight in the control (top) and after RNAi KD of *shakB*-encoded electrical synapses (DLM-Split-GAL4>UAS-shakB-RNAi, middle) and overexpression of ShakB in MN1–5 (bottom). The black arrows mark MN4 and MN5 spikes, and the red arrows indicate simultaneous MN4–MN5 spikes. **b**, Phase histograms of the occurrence of MN5 spikes (*y* axis) in relation to consecutive MN4 spikes (phase $\varphi = 0$ corresponds to the MN4 spike) for control (top), *shakB* KD (middle) and ShakB overexpression (bottom) with a magnified view (inset) ($n = 10$ animals for each genotype). Data are mean (coloured bars) ± s.e.m. (grey). **c**, MN1–5 dye coupling in the *dfmr1* RNAi KD background to increase dye uptake[28]. Scale bar, 20 µm. **d**–**h**, Intracellular recordings of MN pairs. **d**, Hyperpolarizations and depolarizations were conducted bidirectionally (from cell 1 to cell 2 and vice versa). **e**, Increasing current injection amplitude (top trace) increases response amplitudes in electrically coupled MNs (bottom trace). **f**, Plotting the mean presynaptic voltage (V_m) area against the mean postsynaptic voltage area (left) reveals linear relationships, but regression slopes differ between distinct MN pairs (5 animals with strong coupling between the MN1–MN2 and MN3–MN4 pairs; 10 animals with weak coupling between the MN1–MN3, MN1–MN4, MN2–MN3 and MN2–MN4 pairs). The mean CC (postsynaptic peak voltage divided by presynaptic peak voltage; right) differs significantly between MN1–MN2, MN3–MN4 (red, 6 pairs) and all other pairs (green, 10 pairs). Data are mean ± s.e.m. (left) and mean ± s.d. (right). **g**, RNAi KD of *shakB* eliminates detectable electrical coupling between MNs (3 animals). **h**, The CC for the spike AHP is higher than for the spike overshoot. **i**, Firing of a coupled MN ceases during the AHP of the presynaptic MN.

MN. The relationship between presynaptic and postsynaptic charge is linear (Fig. 2e,f). Bidirectional, because the direction of charge transfer can be reversed (Fig. 2d). Compared with common CCs (postsynaptic charge/presynaptic charge[29]) estimated in different types of neurons[29] (0.02–0.2), electrical synapses between the five MNs are weak, but coupling is twice as strong for the MN1–MN2 and MN3–MN4 pairs (coupling coefficients (CC) = 0.023 ± 0.003) compared with all of the other possible combinations of MN1–4 pairs (CC = 0.01 ± 0.0027; Fig. 2f).

The possibility that electrical synapses may desynchronize neural networks under specific conditions has been suggested by theoretical work[30–33]. Experimentally, a transient desynchronization of electrically coupled cerebellar Golgi cells has been described in one study, but for the specific condition of sparse input[34]. There, the transient desynchronization is attributed to a more effective gap junctional transmission of the afterhyperpolarization (AHP) of the action potential compared with its depolarizing overshoot[34]. Similarly, we found that the AHP of MN spikes is transmitted more effectively (CC, 0.042 ± 0.04) through ShakB-mediated electrical synapses than the brief spike overshoot (CC, 0.01 ± 0.004; Fig. 2h). CCs can differ for different components of the action potential because the duration of the presynaptic signal and the time constant of the postsynaptic membrane shape the junction potential[29]. Paired in situ current-clamp recordings of MNs that were induced to fire tonically by somatic current injection indicate that firing of one MN can depress firing of the other during and shortly after the AHP (Fig. 2i). However, the preconditions for desynchronization, as described for electrically coupled cerebellar Golgi cells[34], are probably not fulfilled in the insect asynchronous flight CPG. First, network desynchronization by electrical synapses during flight is not transient but permanent. Second, network desynchronization manifests not only under sparse synaptic input regimes, but through the full range of synaptic input that occurs during flight. Thus, although we cannot rule out a contribution of the AHP, a general mechanism for small network desynchronization without a pronounced AHP (which is probably not sufficient; see above) or inhibitory synapses (not necessary for MN desynchronization; Extended Data Fig. 6e,f) is required. Indeed, theoretical considerations of network connectivity as well as cell-intrinsic excitability provide insights into how the observed splay states are generated.

Coupling strength and excitability class

According to the theory of coupled phase oscillators, splayed-out network states are obtained if pairs of neurons have a preference to fire out of phase, that is, they are phase-repulsive[24]. However, for networks of more than two neurons, a strict antiphase state that maximizes the difference between the firing phases of two neurons cannot be achieved across all neuronal pairs; these systems are therefore called frustrated[35,36]. Typically, they can organize into a splay state that equidistantly maximizes phase distances among neurons to minimize frustration. The phase difference between individual pairs of neurons is therefore not maximal (that is, smaller than half the ISI), but firing phases of neuron pairs are still separated across the population of cells, which reflects the splay state that we observe in vivo (Fig. 1a,f,g and Extended Data Figs. 1 and 6a–d).

Whether pairs of neurons tend to fire out of phase depends on the specific combination of synaptic connectivity and cellular excitability (in other words, the dynamics of action potential generation). Cellular excitability classes characterize qualitatively different types of spiking dynamics and are associated with distinct mathematical bifurcation types at spike onset (that is, threshold). Given the weak electrical coupling among MN1–5, in theory, repulsive phase coupling[24,33,37,38] can be fostered by specific excitability classes. To examine this hypothesis, we use a three-dimensional conductance-based neuron model fitted to MN sodium and delayed rectifier ion channel kinetics[39] (Methods)

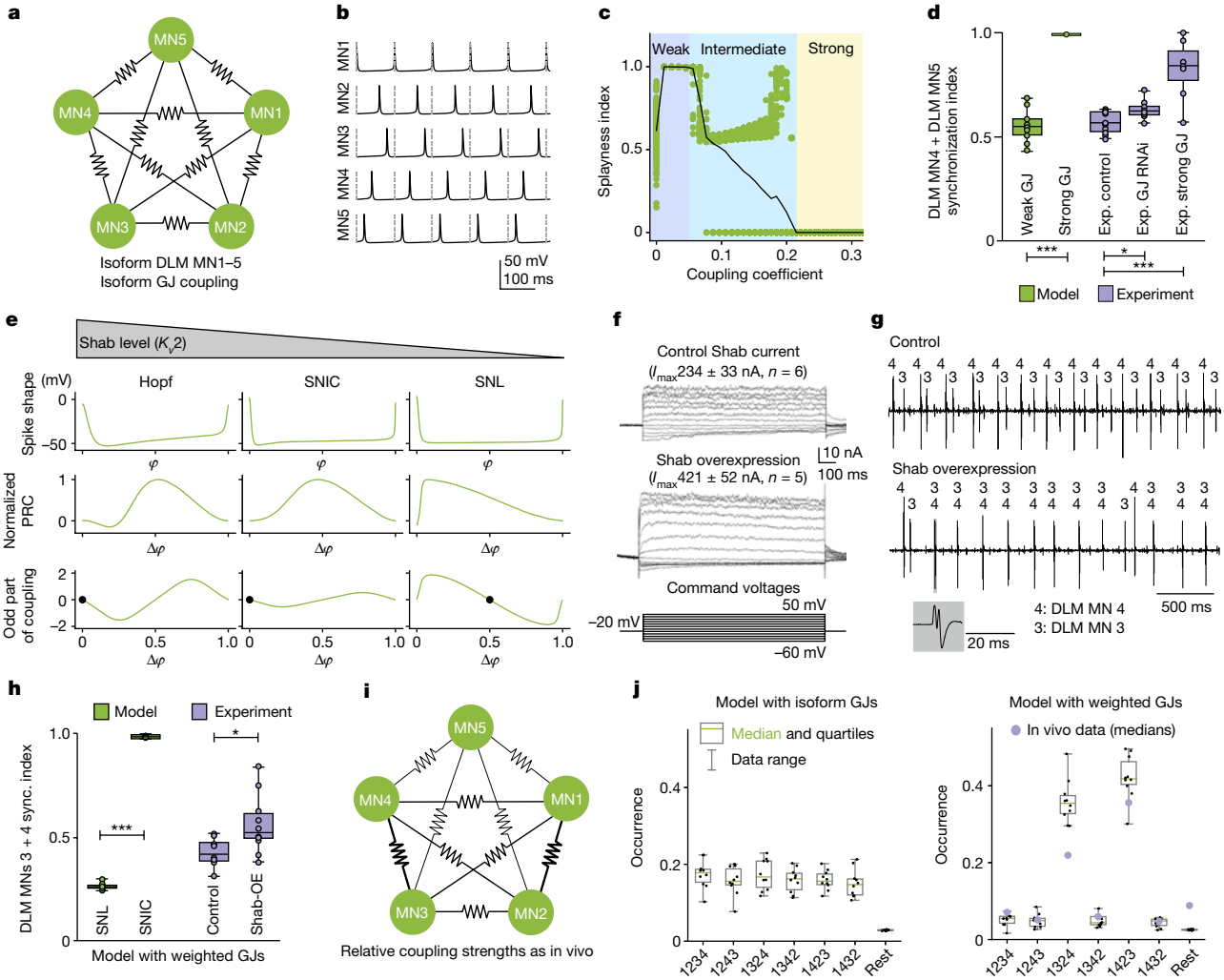

Fig. 3 | Weak electrical synapses and saddle homoclinic orbit (HOM) excitability dynamics underlie firing desynchronization. a,**b**, Conductance-based model with identical gap junctions (GJs, coupling coefficient CC < 0.05) between MN1–5 (**a**) produces splayed-out firing (**b**). **c**, Weak CCs (<0.05) cause high splayness indices (Methods); intermediate CCs (0.05–0.21) decrease splayness and yield multiple stable network states; CCs of >0.21 yield network synchrony (splayness = 0; 200 simulations per CC, green dots; the black line shows the average). **d**, Quantification of 60 s simulations (green, 10 simulations per condition) with a weak CC (0.005) yields significantly lower MN4–MN5 synchronization indices (Methods; median = 0.54) compared with strong coupling (CC = 0.258; median = 1.0; two-sided Mann–Whitney *U*-test, $P = 0.0002$). Similarly, experimental (exp.; purple) synchronization indices are significantly lower in the controls (median = 0.56, 11 animals) compared with the ShakB-overexpression group (median = 0.84, 7 animals, $P = 0.0008$). **e**, Increasing Shab channel levels transforms the single-MN model dynamics from HOM near the SNL point through SNIC to Hopf types (Extended Data Fig. 9a), which vary in action potential waveform (top) and PRC (middle). Averaging theory (Methods and equation (4)) yields the odd part of the coupling function (bottom) for each phase distance $\Delta\varphi$, of which the fixpoints (black dots) determine stable network states. Only the SNL type yields one stable fixpoint at phase 0.5, therefore favouring anti-phase firing. **f**–**h**, Shab overexpression in MN1–5 nearly doubles Shab current (**f**), which causes in-phase firing of the MN3–MN4 pair (**g**) and significantly (two-sided Mann–Whitney *U*-test, $P = 0.0434$) increased synchronization indices (median = 0.52, 10 animals) compared with the controls (median = 0.43, 8 animals) (**h**). Similarly, increasing Shab in models with weighted GJs (as in Fig. 3i) significantly increased MN3–MN4 synchronization (sync.) indices (median = 0.99, $P = 0.0002$). **i**,**j**, Network models with heterogenous CCs (**i**) as found in vivo (Fig. 2f) yield preferred splay states as in animals (**j**, right; 10 simulations per condition; 8 animals, the purple dots depict median values of in vivo data), whereas homogenous coupling does not (**j**, left). For the box plots in **d**, **h** and **j**, the median (centre line), quartiles (box limits) and range (whiskers) are shown.

to generate a gap junctional network of MN1–5 (Fig. 3a). Subjecting the single neuron model to a mathematical bifurcation analysis within the physiological parameter range identified a cellular excitability class that our analysis predicts to favour out-of-phase firing (through a homoclinic spike-onset near the saddle-node loop (SNL) bifurcation; Methods and Extended Data Fig. 9a). Indeed, five identically, weakly electrically coupled MNs with cellular dynamics near the SNL point robustly exhibit a desynchronized splay state (Fig. 3b). Note that the minimal conductance-based model does not contain a pronounced AHP (Fig. 3b (spike shape)), showing that the presynaptic AHP is not mandatory for network desynchronization.

By contrast, systematic variation in electrical coupling strength reveals that weak electrical coupling is required because models with non-zero, small CCs (<0.05), as obtained in vivo (Fig. 2f), yield splayed-out firing (Fig. 3c), whereas, for CCs between 0.05 and 0.21, network in-phase synchronization increases and, for CCs of >0.21, the network state is synchronized (Fig. 3c). To test these model predictions experimentally, we manipulated gap-junction strength genetically and quantified the synchrony of the MN4–MN5 pair from in vivo recordings during flight (Fig. 3d). In control animals with weak gap junctions, the synchronization index (Methods) is low, similar to model simulations with weak gap junctions. RNAi KD of electrical synapses increases

synchronization in vivo (Fig. 3d), underscoring that gap junctions are required for desynchronization. Finally, the model predicts synchrony for strong electrical coupling. Indeed, strengthening of electrical coupling by ShakB overexpression significantly increases synchrony in vivo (Fig. 3d; see also Fig. 2b). Thus, weak electrical coupling is required for network desynchronization.

The mechanistic core of the splay state

We next examined why cellular excitability dynamics close to the SNL point favour splay states. For regularly firing cells with all-or-none action potentials, three main dynamical excitability classes—shaped by cell-intrinsic properties including the ion channel composition—exist[40]. Mathematically, these correspond to three distinct spike-onset bifurcations: the subcritical Hopf, the saddle-node-on-an-invariant cycle (SNIC) and the saddle homoclinic orbit (HOM) bifurcations (Fig. 3e (top row)), which in turn qualitatively determine the phase dependence of a neuron's sensitivity to inputs (also termed the phase-response curve (PRC)) in a bifurcation-specific and, therefore, excitability-class-specific manner (Fig. 3e (middle row)). For the network state, the coupling function, which combines the influence of the PRC and electrical coupling, is decisive (definitions are provided in the Methods), therefore assigning a direct impact on network dynamics to both gap junctions and cellular voltage dynamics[38]. Specifically, an asymmetry of the PRC shape favours stable phase relationships of spiking in the network; these are predicted by the fixpoints of the coupling function's odd part (that is, fixpoints that can be read off the asymmetric components of the function; Methods). Our analysis shows that, for weak reciprocal electrical coupling, out-of-phase firing of identical neurons can be obtained only in combination with a PRC that is monotonically decreasing around phase 0.5 (a graphical explanation is provided in Extended Data Fig. 9b,c). Such a PRC is found for HOM excitability, including dynamics close to the border of SNIC firing, the latter corresponding to the SNL point introduced above (Fig. 3e (middle row)). Here, weak electrical coupling combined with such cellular dynamics results in a stable fixpoint at out-of-phase firing (Fig. 3e (bottom row)). By contrast, for the other two spike-onset bifurcations, synchronous in-phase firing is expected (compare also the stable fixpoints for the phases between neurons; Fig. 3e (bottom row)). Precisely, we predict that MN1–5 should dynamically reside close to the SNL point. Here, the PRC shape enables a network splay state, yet the slope of the neurons' firing-rate versus current-input (*f*–*I*) curves is not as steep as deeper in the HOM regime, therefore enabling smooth control of MN firing frequency and wingbeat power, as observed in vivo (Fig. 1c–e).

To test this model prediction, the excitability class of MN1–5 has to be manipulated in vivo. Shab potassium channels constitute around 50% of the delayed rectifier current in these MNs (Extended Data Fig. 10). Bifurcation analysis of the single-cell MN model reveals an SNL bifurcation (Extended Data Fig. 9a). Moreover, increases in total Shab channel conductance, g_{shab}, induce several transitions in excitability class[37], from HOM (at low g_{shab}), through the SNL point into a SNIC (medium g_{shab}) and a Hopf bifurcation (high g_{shab}, Fig. 3e and Extended Data Fig. 9a). At both excitability dynamics resulting from higher g_{shab} (SNIC and Hopf), the weakly coupled MN1–5 network exhibits a synchronized state, whereas SNL dynamics favour splay states (as described above). We tested this model prediction experimentally by genetic manipulation in vivo. Targeted overexpression of Shab in MN1–5 causes a near doubling of Shab delayed rectifier current (Fig. 3f) without compensatory changes in the amplitudes of non-Shab delayed rectifier current (Extended Data Fig. 10). Recordings of the MN3–MN4 pair were used to test whether this caused firing synchronization in vivo. In controls, both MNs fire out of phase (Fig. 3g (top) and Extended Data Fig. 1). By contrast, with Shab overexpression, the MN3–MN4 pair shows markedly increased synchronization (Fig. 3g (bottom)). Variability in synchronization strength between animals (Fig. 3h) is probably caused by different overexpression strengths and variable levels of other delayed rectifier channels. We also cannot exclude some compensatory regulation of yet other currents. However, pooling the data from all recordings ($n = 10$) revealed a significant increase in firing synchrony after overexpression of Shab (Fig. 3h), as predicted by an increase in g_{shab} in the network model (Fig. 3h). By contrast, our model predicts that a decrease in g_{shab} shifts MNs deeper into the HOM regime but does not cause a transition in excitability class (Fig. 3e and Extended Data Fig. 9a). Thus, with reduced g_{shab} in MN1–5, the network model predicts desynchronization (Fig. 3e). We tested this prediction experimentally. Compared with the control ($n = 7$ animals) targeted RNAi KD of *Shab* in MN1–5 ($n = 11$ animals) reduced the Shab current by around 70% (Extended Data Fig. 10). Paired in vivo recordings of MN4 and MN5 during flight confirm a low synchronization index as predicted by the model (median synchronization indices are 0.559 for control flies ($n = 11$ animals) and 0.598 for *Shab* KD ($n = 11$) and were not statistically different; $P = 0.393$, $U = 74$, two sided Mann–Whitney *U*-test).

The theoretical principles underlying this mechanism are independent of model details (instead they depend on the dynamical excitability class). Weak electrical coupling between neurons with SNL excitability therefore provides a generic mechanism that suffices to produce the observed desynchronized (splay) states in small networks. Importantly, this mechanism holds across different firing rates and does not require a pronounced AHP, but the AHP may further stabilize desynchronization. Although previous studies have provided mechanisms by which networks with electrically coupled neurons can be configured into desynchronized, phase-locked firing[41]—such as inhibitory synapses overriding the synchronization by electrical synapses[42] or interacting with the spiking synchrony[43,44], silencing of electrical synapses in a network with mixed chemical and electrical synapses[42,45], or strongly asymmetric electrical synapses and specific input regimes[46]—desynchronization by the electrical synapse alone, without the need of additional chemical synapses, other network motives or feedback from the network, is conceptually new.

Sequence preference requires heterogenous coupling

Our in vivo recordings show that MN1–5 firing is not only desynchronized, but organized into preferred sequences of cellular activation (within the splay state; Fig. 1f,g). This raises of the question of how the preferred sequences are generated. Our modelling (5 min simulations in network models with SNL neurons and noise) demonstrates that homogenous electrical coupling does not show sequence preference (Fig. 3j (left)). By contrast, heterogenous electrical coupling between MN1–5 (Fig. 3i) as observed in situ (Fig. 2f) produces the same preferred splay states with similar sequence statistics (Fig. 3j (right)) as observed in vivo across animals (Fig. 1f). We conclude that heterogenous weak electrical coupling among neurons with HOM excitability (near SNL) sufficiently explains the preferred splay states in this small network.

Splay state serves stable wing power

MN1–5 splayed-out firing in multiple species suggests that it provides a functional benefit. We tested this hypothesis by comparing the wingbeat frequency between normal splay state and synchronous MN firing, the latter induced by increasing electrical coupling through genetic manipulation (Figs. 2a and 3c). In vivo, synchronous MN firing causes 8× higher wingbeat frequency fluctuations over time compared with firing in splay state (Fig. 4a). The amplitudes of such fluctuations are close to changes in wingbeat frequency in response to optomotor input[1,16] and are therefore functionally relevant for flight altitude control. In the steady-state, muscular stretch sensitivity and wingbeat frequency are directly proportional to the myoplasmic calcium levels[1], but the

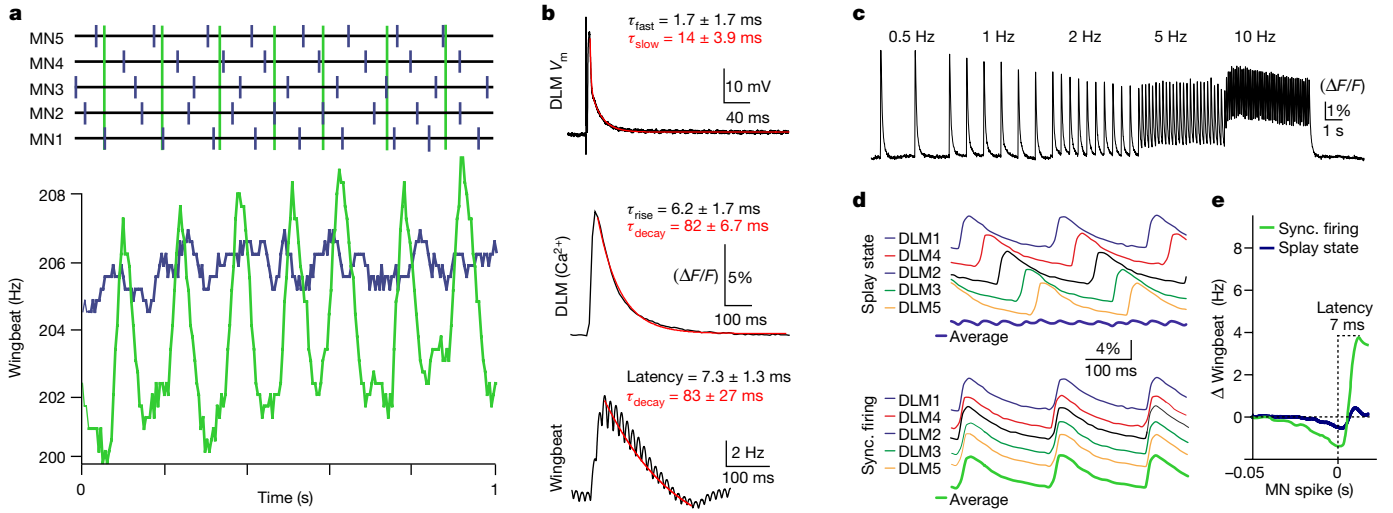

Fig. 4 | Splayed-out firing ensures stable wingbeat power. a, Representative traces of wingbeat and MN multiple-unit recordings during flight (7 animals in each condition). Synchronous MN firing (top, green) causes around eight times larger fluctuations in wingbeat frequency (bottom, green) compared with splayed-out firing (blue). **b**, DLM fibre voltage response to one MN spike is fast (top; decay τ_{fast} ~1.7 ms, τ_{slow} ~14 ms; 3 animals). Both the resulting myoplasmic calcium signal (middle; GCaMP8f $\Delta F/F$; rise $\tau = 6.2 \pm 1.7$ ms; decay $\tau = 82 \pm 6.7$ ms; 7 animals) and wingbeat frequency changes after MN spiking (bottom; latency = 7.3 ± 1.3 ms; decay $\tau = 83 \pm 27$ ms; 7 animals) follow similar slower time courses. **c**, DLM6 calcium responses to different MN5 firing frequencies (Supplementary Video 4). **d**, As each DLM fibre is innervated by one MN, splayed-out firing must result in time-shifted calcium responses (top), but synchronous MN firing results in time-locked calcium responses across fibres (bottom). The resulting average myoplasmic calcium levels across all fibres is considerably larger for synchronous (bottom panel, bottom trace) compared with for splayed-out firing (top panel, bottom trace). **e**, As a result, during flight, splayed-out firing is accompanied by small transient fluctuations in wingbeat frequency (blue; $n = 7$ animals) but synchronous firing is accompanied by significantly ($P = 0.0010$, two-sided unpaired t-test) larger fluctuations with a latency of around 7 ms after each MN spike (green; $n = 7$ animals).

dynamics of myoplasmic calcium in DLM fibres is unclear. To link MN firing patterns to wingbeat frequency, we measured the kinetics of muscle fibre membrane potential and myoplasmic calcium concentration changes after MN1–5 firing (Fig. 4b). An MN spike causes a rapid depolarization of the DLM fibre membrane (Fig. 4b (top)), which is followed by a myoplasmic calcium signal with a rise time constant of around 6 ms and a decay time constant of about 80 ms (Fig. 4b (middle)). If muscular stretch sensitivity was controlled by the myoplasmic calcium levels with a ms temporal resolution, changes in wingbeat frequency during simultaneous MN firing should follow the same time course as changes in myoplasmic calcium across all six DLM fibres. This is precisely what we found (Fig. 4b (bottom)). Synchronous MN firing causes peak wingbeat frequencies after 7.3 ± 1.3 ms (myoplasmic calcium rise time constant $\tau = 6.2 \pm 1.7$ ms) that decline with a time constant $\tau = 83 \pm 27$ ms (calcium decay time constant is 82 ± 6.7 ms).

To determine the kinetics of myoplasmic calcium also at different MN firing frequencies, we stimulated a single MN electrically at different frequencies (0.5, 1, 2, 5, 10 Hz), spanning the normal range during flight, and imaged the resulting calcium signals in the respective DLM target fibre. Discrete myoplasmic calcium signals were observed for the entire frequency range tested (Fig. 4c and Supplementary Video 4), although summation as caused by an incomplete return to resting calcium levels between MN spikes starts at 2 Hz and increases at higher frequencies. However, for firing frequency ranges of MN1–5 that are observed during normal flight (Fig. 1c), in each muscle fibre, myoplasmic calcium fluctuates around each corresponding MN spike. Given that we did not observe any differences in the temporal coupling of MN firing and myoplasmic calcium across different stimulation frequencies or different DLM fibres, these data can be extrapolated to all DLM fibres for splay state (Fig. 4d (top)) as compared to synchronous MN firing (Fig. 4d (bottom)). Given that each DLM fibre is innervated by one MN only (Fig. 1a), MN firing in splay state causes splayed-out calcium signals across the different muscle fibres (Fig. 4d (top)), each peaking around 6 ms after the respective MN spike and declining with a time constant of around 80 ms (Fig. 4b (middle)). The bottom trace shows the resulting average myoplasmic calcium across fibres (Fig. 4d (top)). By contrast, during synchronous firing of MN1–5, the calcium signals in all DLM fibres are time locked, which results in much larger calcium fluctuations across DLM fibres (Fig. 4d (bottom)). This extrapolation of the average myoplasmic calcium levels across the DLM fibres predicts eightfold smaller fluctuations in wingbeat frequency over time in normal splay state than for synchronous MN firing. We confirmed this prediction by averaging changes in wingbeat frequency around MN spikes for splayed-out (Fig. 4e (blue line)) as opposed to synchronous firing (Fig. 4e (green line)). Thus, the splay state serves to minimize wing power fluctuations.

Taken together, splay-state asynchronous flight motor patterns are conserved across individuals and species, are produced by a minimal CPG of weakly electrically coupled MNs, and serve constant wingbeat power output at a given power demand. This provides a comprehensive view of the asynchronous flight CPG network structure and the resulting functional consequences for one of the most abundant forms of locomotion on earth. Moreover, we provide a theoretical background for firing d esynchronization/synchronization in small gap-junctional networks in the context of their specific cellular excitability. The underlying mechanism is generic, predicting desynchronizing functions of electrical synapses beyond the motor system of insects. Electrical synapses can therefore be used for operations such as sign-reversal and ensemble firing desynchronization, a functional versatility and impact on neural circuit dynamics that was previously attributed to chemical synapses alone.

Online content

Any methods, additional references, Nature Portfolio reporting summaries, source data, extended data, supplementary information, acknowledgements, peer review information; details of author contributions and competing interests; and statements of data and code availability are available at https://doi.org/10.1038/s41586-023-06099-0.

1. Gordon, S. & Dickinson, M. H. Role of calcium in the regulation of mechanical power in insect flight. *Proc. Natl Acad. Sci. USA* **103**, 4311–4315 (2006).
2. Frye, M. et al. Molecular dynamics of cyclically contracting insect flight muscle in vivo. *Nature* **433**, 330–334 (2005).
3. Iwamoto, H. & Yagi, N. The molecular trigger for high-speed wing beats in a bee. *Science* **341**, 1243–1246 (2013).
4. Fry, S. N., Sayaman, R. & Dickinson, M. H. The aerodynamics of free-flight maneuvers in *Drosophila*. *Science* **300**, 495–498 (2003).
5. Farisenkov, S. E. et al. Novel flight style and light wings boost flight performance of tiny beetles. *Nature* **602**, 96–100 (2022).
6. Stork, N. E. How many species of insects and other terrestrial arthropods are there on Earth? *Annu. Rev. Entomol.* **63**, 31–45 (2018).
7. Deora, T., Gundiah, N. & Sane, S. P. Mechanics of the thorax in flies. *J. Exp. Biol.* **220**, 1382–1395 (2017).
8. Josephson, R. K., Malamud, J. G. & Stokes, D. R. Asynchronous muscle: a primer. *J. Exp. Biol.* **203**, 2713–2722 (2000).
9. Ikeda, J. H. & Koenig, J. H. Morphological identification of the motor neurons innervating the dorsal longitudinal flight muscle of *Drosophila melanogaster*. *J. Comp. Neurol.* **273**, 436–444 (1988).
10. Coggshall, J. C. Neurons associated with the dorsal longitudinal flight muscles of *Drosophila melanogaster*. *J. Comp. Neurol.* **177**, 707–720 (1978).
11. Consoulas, C., Restifo, L. L. & Levine, R. B. Dendritic remodeling and growth of motoneurons during metamorphosis of *Drosophila melanogaster*. *J. Neurosci.* **22**, 4906–4917 (2002).
12. Tyrer, N. M. & Altman, J. S. Motor and sensory flight neurons in a locust demonstrated using cobalt chloride. *J. Comp. Neurol.* **157**, 117–138 (1974).
13. Duch, C., Bayline, R. J. & Levine, R. B. Postembryonic development of the dorsal longitudinal flight muscle and its innervation in *Manduca sexta*. *J. Comp. Neurol.* **422**, 1–17 (2000).
14. Schlurmann, M. & Hausen, K. Motoneurons of the flight power muscles of the blowfly *Calliphora erythrocephala*: structures and mutual dye coupling. *J. Comp. Neurol.* **500**, 448–464 (2007).
15. Harcombe, E. S. & Wyman, R. J. Output pattern generation by *Drosophila* flight motoneurons. *J. Neurophysiol.* **40**, 1066–1077 (1977).
16. Ryglewski, S. et al. Dendrites are dispensable for basic motoneuron function but essential for fine tuning of behavior. *Proc. Natl Acad. Sci. USA* **111**, 18049–18054 (2014).
17. Wang, Q., Zhao, C. & Swank, D. M. Calcium and stretch activation modulate power generation in *Drosophila* flight muscle. *Biophys. J.* **101**, 2207–2213 (2011).
18. Harcombe, E. S. & Wyman, R. J. The cyclically repetitive firing sequences of identified *Drosophila* flight motoneurons. *J. Comp. Physiol.* **123**, 271–279 (1978).
19. Selverston, A. I. Invertebrate central pattern generator circuits. *Philos. Trans. R. Soc. B* **365**, 2329–2345 (2010).
20. Kiehn, O. Decoding the organization of spinal circuits that control locomotion. *Nat. Rev. Neurosci.* **17**, 224–238 (2016).
21. Ryglewski, S., Vonhoff, F., Scheckel, K. & Duch, C. Intra-neuronal competition for synaptic partners conserves the amount of dendritic building material. *Neuron* **93**, 632–645 (2017).
22. Koenig, J. H. & Ikeda, K. Neural interactions controlling timing of flight muscle activity in *Drosophila*. *J. Exp. Biol.* **87**, 121–136 (1980).
23. Koenig, J. H. & Ikeda, K. Reciprocal excitation between identified flight motor neurons in *Drosophila* and its effect on pattern generation. *J. Comp. Physiol. A* **150**, 305–317 (1983).
24. Coombes, S. Neuronal networks with gap junctions: a study of piecewise linear planar neuron models. *SIAM J. Appl. Dyn. Syst.* **7**, 1101–1129 (2008).
25. Phelan, P. Innexins: members of an evolutionarily conserved family of gap-junction proteins. *Biochim. Biophys. Acta* **1711**, 225–245 (2005).
26. Goodenough, D. A. & Paul, D. L. Gap junctions. *Cold Spring Harb. Perspect. Biol.* **1**, a002576 (2009).
27. Connors, B. W. Synchrony and so much more: diverse roles for electrical synapses in neural circuits. *Dev. Neurobiol.* **77**, 610–624 (2017).
28. Kennedy, T. & Broadie, K. Fragile X mental retardation protein restricts small dye iontophoresis entry into central neurons. *J. Neurosci.* **37**, 9844–9858 (2017).
29. Alcamí, P. & Pereda, A. E. Beyond plasticity: the dynamic impact of electrical synapses on neural circuits. *Nat. Rev. Neurosci.* **20**, 253–271 (2019).
30. Chow, C. C. & Kopell, N. Dynamics of spiking neurons with electrical coupling. *Neural Comput.* **12**, 1643–1678 (2000).
31. Lewis, T. J. & Rinzel, J. Dynamics of spiking neurons connected by both inhibitory and electrical coupling. *J. Comput. Neurosci.* **14**, 283–309 (2003).
32. Ostojic, S., Brunel, N. & Hakim, V. Synchronization properties of networks of electrically coupled neurons in the presence of noise and heterogeneities. *J. Comput. Neurosci.* **26**, 369–392 (2009).
33. Han, S. K., Kurrer, C. & Kuramoto, Y. Dephasing and bursting in coupled neural oscillators. *Phys. Rev. Lett.* **75**, 3190–3193 (1995).
34. Vervaeke, K. et al. Rapid desynchronization of an electrically coupled interneuron network with sparse excitatory synaptic input. *Neuron* **67**, 435–451 (2010).
35. Zanette, D. H. Synchronization and frustration in oscillator networks with attractive and repulsive interactions. *Europhys. Lett.* **72**, 190–196 (2005).
36. Zillmer, R., Livi, R., Politi, A. & Torcini, A. Stability of the splay state in pulse-coupled networks. *Phys. Rev. E* **76**, 046102 (2007).
37. Hesse, J., Schleimer, J.-H. & Schreiber, S. Qualitative changes in phase-response curve and synchronization at the saddle-node-loop bifurcation. *Phys. Rev. E* **95**, 052203 (2017).
38. Hesse, J., Schleimer, J.-H., Maier, N., Schmitz, D. & Schreiber, S. Temperature elevations can induce switches to homoclinic action potentials that alter neural encoding and synchronization. *Nat. Commun.* **13**, 3934 (2022).
39. Berger, S. D. & Crook S. M. Modeling the influence of ion channels on neuron dynamics in *Drosophila*. *Front. Comput. Neurosci.* **9**, 139 (2015).
40. Izhikevich, E. M. *Dynamical Systems in Neuroscience* (MIT Press, 2007).
41. Marder, E., Gutierrez, G. J. & Nusbaum, M. P. Complicating connectomes: electrical coupling creates parallel pathways and degenerate circuit mechanisms. *Dev. Neurobiol.* **77**, 597–609 (2017).
42. Marder, E. Roles for electrical coupling in neural circuits as revealed by selective neuronal deletions. *J. Exp. Biol.* **112**, 147–167 (1984).
43. Weaver, A. L., Roffman, R. C., Norris, B. J. & Calabrese, R. L. A role for compromise: synaptic inhibition and electrical coupling interact to control phasing in the leech heartbeat CPG. *Front. Behav. Neurosci.* **4**, 38 (2010).
44. Gutierrez, G. J., O'Leary, T. & Marder, E. Multiple mechanisms switch an electrically coupled, synaptically inhibited neuron between competing rhythmic oscillators. *Neuron* **77**, 845–858 (2013).
45. Johnson, B. R., Peck, J. H. & Harris-Warrick, R. M. Amine modulation of electrical coupling in the pyloric network of the lobster stomatogastric ganglion. *J. Comp. Physiol. A* **172**, 715–732 (1993).
46. Sevetson, J. & Haas, J. S. Asymmetry and modulation of spike timing in electrically coupled neurons. *J. Neurophysiol.* **113**, 1743–1751 (2015).

LETTERS

Sensitivity to perturbations *in vivo* implies high noise and suggests rate coding in cortex

Michael London[1], Arnd Roth[1], Lisa Beeren[1], Michael Häusser[1] & Peter E. Latham[2]

It is well known that neural activity exhibits variability, in the sense that identical sensory stimuli produce different responses[1–3], but it has been difficult to determine what this variability means. Is it noise, or does it carry important information—about, for example, the internal state of the organism? Here we address this issue from the bottom up, by asking whether small perturbations to activity in cortical networks are amplified. Based on *in vivo* whole-cell patch-clamp recordings in rat barrel cortex, we find that a perturbation consisting of a single extra spike in one neuron produces approximately 28 additional spikes in its postsynaptic targets. We also show, using simultaneous intra- and extracellular recordings, that a single spike in a neuron produces a detectable increase in firing rate in the local network. Theoretical analysis indicates that this amplification leads to intrinsic, stimulus-independent variations in membrane potential of the order of ±2.2–4.5 mV—variations that are pure noise, and so carry no information at all. Therefore, for the brain to perform reliable computations, it must either use a rate code, or generate very large, fast depolarizing events, such as those proposed by the theory of synfire chains[4,5]. However, in our *in vivo* recordings, we found that such events were very rare. Our findings are thus consistent with the idea that cortex is likely to use primarily a rate code.

The brain, like all physical devices, operates in the presence of noise. Nevertheless, it performs complex computations with amazing speed and accuracy, in some cases reaching fundamental physical limits set by its sensors[6]. Clearly, the brain has devised computational strategies, and a neural code, that are robust to noise. Understanding the structure of that noise should shed light on both.

The traditional experimental approach to studying noise in cortical sensory areas is to present the same stimulus repeatedly to an organism while recording neuronal responses. Such recordings always show substantial trial-to-trial variability[1–3]. However, interpreting that variability has been difficult, as there are two possible sources for it. One is the variability associated with truly random events, such as ion channel noise and stochastic synaptic release. This is intrinsic noise: intrinsic because it cannot be eliminated, and noise because it contributes to the neuronal variability but carries no information whatsoever. The other source of variability is activity from other brain areas. That activity might provide information about, say, the degree of arousal or some other internal state, but it would not be related to the stimulus. This variability is signal, even though it would look like noise to an observer trying to relate the neural activity to the stimulus.

Here we determine a lower bound on the level of intrinsic noise in cortical networks. The lower bound we consider is the trial-to-trial variability that would be observed in a deterministic network that received identical input, down to the last spike, on multiple trials, except for one very brief random event. If the dynamics of the network is such that small differences in activity associated with the single random event lead to very large differences in patterns of neuronal activity, then trial-to-trial variability would, necessarily, be high. If, on the other hand, small differences in activity lead to even smaller differences in patterns of neuronal activity, then trial-to-trial variability can be low.

In our analysis and experiments, the random event is a single extra spike added to a randomly chosen excitatory neuron, as in Fig. 1a. This one extra spike (magenta arrow at time $t = 0$ in Fig. 1a) can produce other extra spikes in its postsynaptic targets (magenta arrows). If it produces more than one, on average, then perturbations would be amplified, and noise would be high (see the steady-state regime in Fig. 1a, b). If, on the other hand, one extra spike produces less than one extra spike, on average, then perturbations would decay, and noise could be small.

To determine the average number of extra postsynaptic spikes produced by a single extra presynaptic spike, we note that it is the product of two numbers: the average number of connections made by each neuron, and the average probability that a unitary synaptic event produces an extra spike.

The first number is known from anatomical studies[7,8] to be between 1,000 and 2,000 (a synaptic connection that gives rise to a unitary excitatory postsynaptic potential (EPSP) can consist of multiple synaptic contacts; here we assume that a neuron makes five synaptic contacts per connection[9]). Thus, one extra spike produces, on average, $1{,}500 \pm 500$ extra EPSPs in the network.

The second number, the probability that a unitary synaptic input produces an extra spike, was determined experimentally. We made whole-cell patch-clamp recordings from layer 5 pyramidal neurons in the barrel cortex of anaesthetized rats while injecting current pulses to generate postsynaptic currents (injected PSCs) of various amplitudes. For each amplitude we constructed a post-stimulus time histogram (PSTH) triggered on the time of the injected current pulses, and used it to deduce the probability of an extra spike. A typical experiment is illustrated in Fig. 2a. In a single trial it is very difficult to tell whether an individual injected PSC has an effect on the probability of an extra spike. The PSTHs, however, reveal a clear signal (Fig. 2b). Integrating the PSTH over a time window of 5 ms, we find that a single input with an amplitude of +25 pA causes the probability of observing a spike to increase by 0.004 (top panel of Fig. 2b), and an input with an amplitude of −25 pA causes the probability to decrease by 0.001 (bottom panel).

Figure 3a shows, for a range of positive and negative injected PSCs, the pooled data from the 40 cells in our data set. There are clear peaks in the PSTHs for positive currents and clear valleys for negative currents. Moreover, the cumulative probability of an extra spike (the integral of the PSTH relative to the mean firing rate) shown below the PSTHs does not return to baseline, indicating that the

[1]Wolfson Institute for Biomedical Research and Department of Neuroscience, Physiology and Pharmacology, University College London, Gower Street, London WC1E 6BT, UK. [2]Gatsby Computational Neuroscience Unit, University College London, Queen Square, London WC1N 3AR, UK.

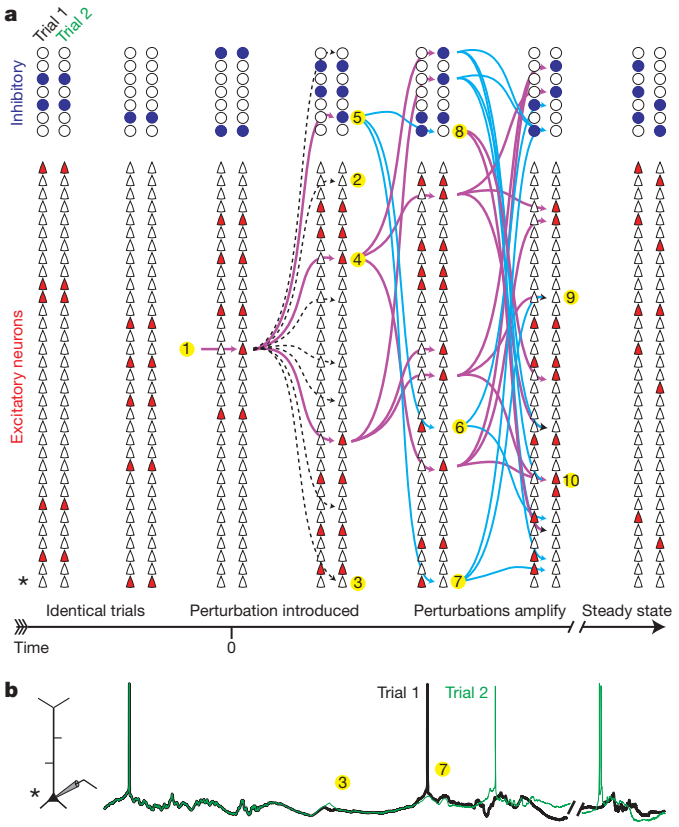

Figure 1 | The effect of an extra spike on a neuronal network. **a**, The propagation of missed and extra spikes in a recurrent network. Each two-column block represents a snapshot of the activity of a population of excitatory and inhibitory neurons on two different trials. Filled neurons are spiking. The trials are identical until time $t = 0$, at which point an extra spike is added to a neuron in trial 2 (point 1). The extra spike has no effect on most of its postsynaptic targets (dashed arrows and 2, 3; omitted subsequently for clarity), but it triggers an extra spike in a fraction of them (magenta arrows and 4, 5). These extra spikes cause a cascade of extra and, as soon as inhibitory neurons are recruited, missed spikes (6–8). Extra inhibitory spikes (5) and missed excitatory spikes (6, 7) are indicated with cyan arrows. The perturbation amplification rate decreases when collisions occur (9, 10), and eventually missed and extra spikes occur at the same rate, resulting in a steady state (rightmost column). **b**, Membrane potential of the bottom neuron (*) on the two trials. The membrane potential is identical until an extra presynaptic spike causes a slight divergence (3). As missed and extra spikes accumulate, the difference grows (7), until it eventually reaches steady state.

peaks are due to changes in net spike output, rather than shifted spikes (all cumulative probabilities are significantly different from zero at the $P = 0.05$ level, except for the last two points of the 25-pA histogram). In Fig. 3b we combine the data from the different current amplitudes and plot probability versus the total charge in the injected current pulses (we use charge rather than amplitude for reasons we discuss shortly).

The results of these experiments provide us with a relation between the size of injected PSCs and the probability of extra spikes *in vivo*. However, what we need is the relation between physiological synaptic inputs (which are generated by conductance changes, typically on dendrites) and the probability of an extra spike. To determine this, we constructed a detailed compartmental model of a pyramidal neuron (see Supplementary Information, section 4), and used it to simulate the effect of conductance changes on the probability of an extra spike. Consistent with theoretical studies[10,11], these simulations show that the probability of an extra spike depends on the total charge arriving at the soma, regardless of whether it is caused by a current injection or a conductance change, and is relatively insensitive to the location of the input (Fig. 3c).

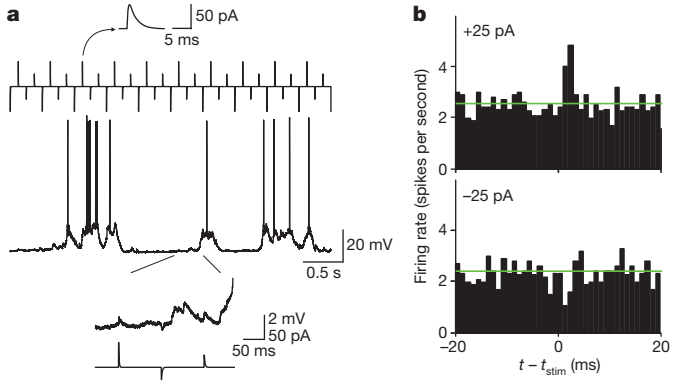

Figure 2 | Small perturbations affect spiking probability *in vivo*. **a**, Positive and negative current pulses (upper trace) were injected via a whole-cell patch-clamp electrode into a pyramidal neuron in rat barrel cortex *in vivo*, and the accompanying membrane potential was recorded (lower trace). **b**, PSTHs triggered on the +25 pA (top) and −25 pA (bottom) current pulses, binned at 1 ms; the green line shows the average firing rate. For this neuron the probability of an extra spike within 5 ms of the current pulse is 0.004 for +25 pA and the probability of a missed spike within 5 ms is 0.001 for −25 pA.

Combining this result with the fact that there is an approximately linear relation between charge and probability (Fig. 3b), we see that the average probability that a unitary synaptic input causes an extra spike is the product of the slope of the positive part of the regression line in Fig. 3b and the average charge associated with a unitary synaptic input *in vivo*. The former we have measured; it is 0.061 ± 0.010, in units of probability/pC (picocoulomb) (Fig. 3b). The latter we estimated from

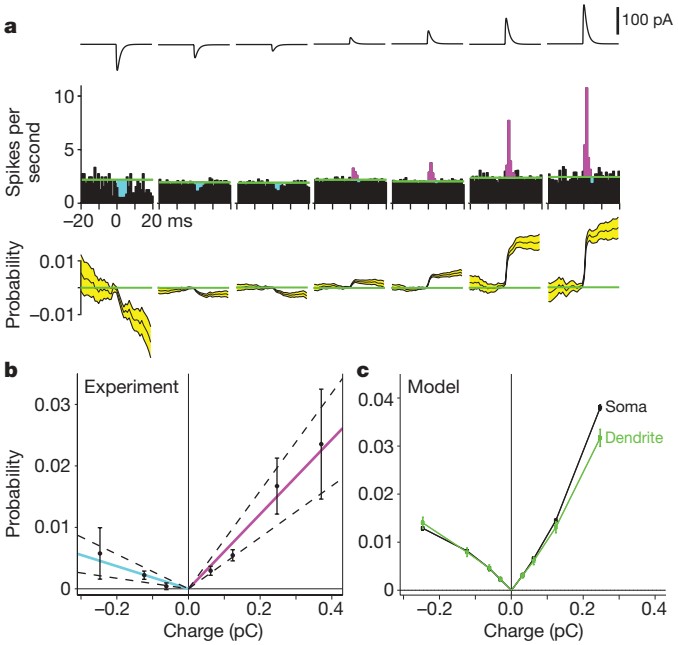

Figure 3 | Determining the sensitivity of neurons to small perturbations *in vivo*. **a**, Top: injected PSCs (experiment as in Fig. 2). Centre: combined PSTHs from 40 experiments, triggered on the current pulses ($t = 0$) and binned at 1 ms. Cyan, missed spikes; magenta, extra spikes; green lines, mean firing rate. Bottom, cumulative probability of an extra spike; yellow, one standard deviation. **b**, Probability of an extra spike within 5 ms of the current pulse versus total injected charge. Magenta and cyan lines, least squares fit to the data; dashed lines, 95% confidence intervals; error bars, standard error of the mean. Positive charge, slope = 0.061 ± 0.010 probability/pC ($P = 5 \times 10^{-9}$); negative charge, slope = −0.018 ± 0.0049 probability/pC ($P = 4 \times 10^{-4}$). **c**, Same as **b** but from simulations of a layer 5 pyramidal neuron (Supplementary Information, section 4, and Supplementary Fig. 3). Black, current injected at the soma; green, current injected at the distal dendrites, 403 μm from the soma.

published data on paired recordings[9,12–14] (data that include synaptic failures). Taking an average across these reports, we find that the average charge associated with a unitary excitatory synaptic input is 0.31 ± 0.07 pC, corresponding to an EPSP of approximately 1 mV (see Supplementary Information, section 4). The product of the two numbers, denoted $\bar{p}_e$, is given by

$$\begin{aligned}\bar{p}_e &= (0.061 \pm 0.010 \text{ probability/pC}) \times \\ &\quad (0.31 \pm 0.07 \text{ pC per unitary synaptic input}) \\ &= 0.019 \pm 0.0053 \text{ probability per unitary synaptic input}\end{aligned}$$

(see Supplementary Information, section 8, for a derivation of confidence limits).

Multiplying $\bar{p}_e$ (0.019 ± 0.0053) by the average number of connections made by each neuron ($1{,}500 \pm 500$) yields 28 ± 13 extra spikes per spike. Thus one extra spike in an excitatory neuron causes, on average, 28 of its postsynaptic neurons to emit an extra spike. This implies very rapid amplification of perturbations, and should quickly disrupt spike patterns across the network. In fact, if the perturbations were to grow unchecked, in just five integration time steps there would be about 17 million extra spikes in the network.

Perturbations do not, of course, grow unchecked. This is because extra and missed excitatory and inhibitory spikes interact: if an extra excitatory and extra inhibitory spike have the same postsynaptic target, they will at least partly cancel each other, thus reducing the probability of either a missed or extra postsynaptic spike (points 9 and 10 in Fig. 1a). As the number of missed and extra spikes grows, cancellation becomes more likely, and eventually the network reaches a steady state in which missed spikes are produced at the same rate, on average, as extra ones (Fig. 1b and Supplementary Fig. 9).

These results suggest that a single extra spike should have a measurable effect on network firing rate. That effect, though, should be small: the approximately 2% increase in firing rate that we saw for connected pairs of neurons (summarized by $\bar{p}_e$ above) is reduced by the low connectivity in somatosensory cortex (approximately 4% (ref. 15)), and spread out by 10–20 ms due to axonal delays, dendritic filtering and latency to spike. Taking these into account quantitatively (Supplementary Information, section 2), we find that a single spike should lead to a local increase in firing rate of 0.04–0.08 Hz.

To test this prediction, we conducted a second series of *in vivo* experiments in which we triggered single spikes in a presynaptic neuron by a whole-cell patch-clamp recording, and simultaneously recorded spikes from a population of neurons in the local network using a 16-channel extracellular electrode array placed in the somatosensory cortex (Fig. 4a, b). We then constructed a PSTH of extracellular spikes triggered on the stimulus (Fig. 4c). As predicted, we observed an increase in firing rate on the extracellular electrodes following the single spike in the stimulated neuron. The increase, as assessed by the cumulative increase in the probability of an extra spike, is statistically significant at the $P = 0.01$ level for greater than 100 ms (Fig. 4d; $n = 10$ experiments). Moreover, in the first 10–20 ms, the increase was 0.03–0.065 Hz (Fig. 4c, inset), very close to the increase of 0.04–0.08 Hz predicted above. Thus, not only does a single extra spike introduced into somatosensory cortex produce a measurable effect on the network that lasts for more than 50 ms, it produces an effect whose size is predicted by our single-neuron current injection experiments.

So far we have focused on the effect of a single spike. Now we turn to the steady state, where the perturbations have stopped growing (so that missed and extra spikes occur at the same rate). How big are the trial-to-trial voltage fluctuations associated with the ongoing missed and extra spikes? This is a critical question, because it is, ultimately, these voltage fluctuations that limit spike timing precision. To answer it, we assume that in steady state there are m missed and extra spikes in a time window that corresponds to a typical neuron's mean integration time, we compute m self-consistently (by demanding that the presynaptic and postsynaptic probabilities of a spike are the same), and then relate it to the size of the voltage fluctuations. The presynaptic probability, denoted p_{pre}, is equal to m/K where K is the average number of presynaptic connections. The postsynaptic probability, denoted p_{post}, is approximately $\sqrt{m}$ times larger than $\bar{p}_e$, the probability associated with one presynaptic spike (assuming that missed and extra spikes are reasonably uncorrelated, invoking central-limit-type arguments and using the linearity of probability versus charge in Fig. 3b). Consequently, $p_{\text{post}} \propto \sqrt{m}\bar{p}_e$. Self-consistency tells us that $p_{\text{pre}} = p_{\text{post}}$, so we arrive at

$$\sqrt{m} \propto K\bar{p}_e \tag{1}$$

Again assuming that the m missed and extra spikes received by a neuron are reasonably uncorrelated, the amplitude of intrinsic voltage fluctuations associated with missed and extra spikes, denoted σ_V, is proportional to $\sqrt{m}\bar{V}_{\text{PSP}}$ where $\bar{V}_{\text{PSP}}$ is the average PSP size. Combining this observation with equation (1), we have

$$\sigma_V \propto K\bar{p}_e\bar{V}_{\text{PSP}} \tag{2}$$

The key point to extract from equation (2) is that the voltage fluctuations are proportional to the growth rate of the perturbations, $K\bar{p}_e$. Because $K\bar{p}_e \approx 28$, we expect the intrinsic voltage fluctuations associated with the growth of perturbations to be large. And, indeed, they are: in Supplementary Information, section 6, we perform a more extensive analysis that takes into account correlations among excitatory and inhibitory neurons as well as saturation of the number of missed and extra spikes, and we verify the analysis with large-scale network simulations. What we find is that the constant of proportionality in equation (2) ranges in our data from 0.08 to 0.16, and so σ_V ranges from about 2.2 to 4.5 mV (Supplementary Fig. 7).

These large trial-to-trial voltage fluctuations indicate that there is a high level of intrinsic noise in the cortex. Therefore rapid depolarizing events, like those postulated for synfire chains[4] or polychronization[5], would be required to produce very precisely timed spikes. Quantitatively, for a given value of the voltage fluctuations, σ_V, a

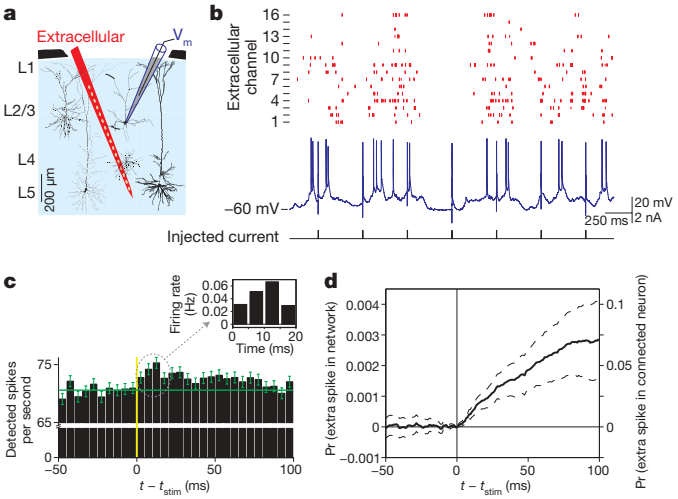

Figure 4 | The effect of one extra spike on network activity *in vivo*. **a**, The recording configuration. The extracellular silicon probe (red) contained 16 recording sites spaced 50 μm apart. The patch electrode (blue) was used to trigger spikes by brief depolarizing current pulses. **b**, Extracellular spikes (top) and intracellular membrane potential (bottom). **c**, PSTH triggered on the stimulus and binned at 5 ms; it includes all extracellular spikes on all electrodes from ten experiments. Error bars are one standard deviation. Inset: change in firing rate per neuron, assuming an average firing rate of 1 Hz (ref. 30). **d**, Cumulative probability of an extra spike, averaged over all recorded neurons, again assuming an average firing rate of 1 Hz. Dashed lines indicate one standard deviation, obtained using bootstrap sampling. Left scale, probability (Pr) of an extra spike in a randomly chosen neuron. Right scale, probability of an extra spike between connected pairs, found by dividing the left side by 0.04, corresponding to the 4% connectivity observed in somatosensory cortex[15].

spike will occur with a precision of $\delta\tau$ ms if the membrane potential changes by $2\sigma_V$ mV in $\delta\tau$ ms (the factor of 2 is necessary to ensure reliability: because σ_V is the standard deviation, the voltage can, with reasonable probability, range from σ_V below the mean to σ_V above it). To determine how often there are voltage excursions that would allow spike timing of precision $\delta\tau$, we examined experimentally recorded voltage traces (Fig. 5a), counted how often the membrane potential changed by $2\sigma_V$ mV in $\delta\tau$ ms, and averaged over our uncertainty in σ_V. The results are shown in Fig. 5b, and indicate that precisely timed events are very rare: events with a precision of $\delta\tau = 1$ ms occur, on average, once every 10,000 seconds per neuron (about once every 3 h); events with a precision of 5 ms occur less than once every 100 seconds per neuron; and events with a precision of 10–20 ms occur less than once every 40 seconds per neuron. In addition, not only are precisely timed events rare, but the rates shown in Fig. 5b constitute an upper bound, because precisely timed events occur by chance at non-zero rates.

Taken together, our results indicate that there is a large amount of intrinsic noise in cortex, and that this noise puts severe constraints on spike timing codes. One potential caveat is that our results were obtained under anaesthesia. The effect of anaesthesia on our estimate of the number of extra spikes per spike is likely to be small, because responsiveness of barrel cortex neurons under the awake and anaesthetized states is similar[16,17]. The frequency of large voltage excursions, on the other hand, may be more sensitive to anaesthesia; in particular, it is possible that the rate of large, fast depolarizing events (Fig. 5b) is simply higher in awake than anaesthetized animals. A second caveat is that our analysis assumed linear synaptic integration. Recent studies show that precisely timed input to dendritic branches can yield precisely timed output spikes in the axon without large somatic sub-threshold voltage excursions[18–21]. These mechanisms, though, have only been demonstrated *in vitro*, and only when input to the dendrites was carefully regulated in both space and time; it remains unclear to what extent these conditions are satisfied *in vivo* (but see ref. 22).

Our study is in line with previous theoretical work that suggests neuronal networks are chaotic[23–26]. However, it is, to our knowledge, the first experimental demonstration of the sensitivity of an intact network to perturbations *in vivo*. We are also the first to explore the consequences of these results for the level of noise in the cortex and its likely effect on the precision of spike timing.

What do our results imply for neural coding? Superficially, it seems natural to conclude that if every spike has a large effect on network activity, then every spike should count, and the brain must be using a very sophisticated neural code in which the time and identity of every spike carries meaningful information. In fact, our results imply just the opposite. This is because network activity is bounded, so growth of perturbations in some dimensions (for example, as measured by trial-to-trial difference in membrane potential) necessarily implies contraction in others[27]. It is this contraction that causes networks to rapidly forget their past. Thus, although an extra spike can radically modify patterns of activity, patterns of activity cannot encode which extra spike caused the modification. The implication, then, is not that rat barrel cortex (and, we suspect, other areas of cortex and other species) must be using a very sophisticated spike timing code, but that it is likely to be using a code that is robust to perturbations, such as a rate code in which it is the average firing rate over large populations of neurons that carries information.

Finally, the fact that studies have found millisecond timing both in anaesthetized and awake animals in the rat barrel cortex[28] as well as in other cortical regions[3,29] is not inconsistent with our results. The precise timing in those studies is associated with a feedforward sweep of activity caused by a rapidly time-varying stimulus. Our results, on the other hand, apply to slowly varying stimuli and higher-order computations, and suggest that in those cases the cortex does not rely on precise spike timing.

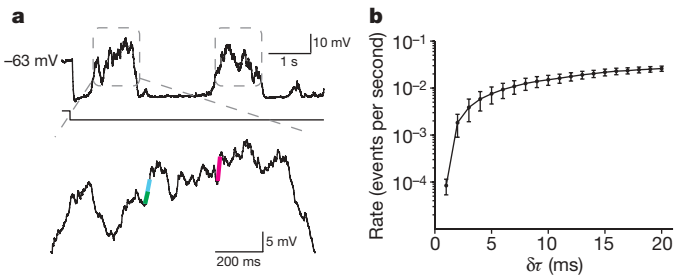

Figure 5 | Precisely timed events are rare. a, Top, example membrane potential recording. A steady current between −250 and −450 pA (bottom trace) was applied to reduce the frequency of action potentials. Bottom: expanded view of an up state. The coloured line segments indicate events of various amplitudes and rise times. Green, amplitude 3 mV, rise time 12 ms; cyan, 6 mV, 20 ms; magenta, 6 mV, 5 ms. **b**, The rate of events with precision $\delta\tau$ (events for which the voltage changed by at least $2\sigma_V$ mV in time $\delta\tau$, averaged over our uncertainty in σ_V, the latter given in Supplementary Fig. 7). Data from nine cells recorded *in vivo*, with events counted only during up states (boxed regions in **a**). Three of the cells received, on alternate trials, sensory stimulation by a slowly rotating (1 Hz) drum of sandpaper. There was no statistically significant difference between event rates with and without whisker stimulation.

METHODS SUMMARY

Sprague-Dawley rats (postnatal day 18–25, average 45.6 g) were anaesthetized with urethane (Sigma; 1.5 g kg^{-1}, intraperitoneally), and *in vivo* whole-cell patch-clamp recordings were made using blind patch techniques. Recordings were made at a depth of 1180 ± 165 μm, and neurons were identified as layer 5 pyramidal cells by input resistance, firing properties and in five cases by cell morphology ($n = 5/5$). For the single-cell experiments, excitatory postsynaptic current (EPSC) waveforms separated by either 100 or 200 ms were injected into the recorded neuron. The rise and decay times of the EPSC waveforms were 0.3 and 1.7 ms, respectively, and the amplitudes alternated between four values, either +50, −25, +25, −50 pA or +100, −50, +50, −100 pA. In some cases, we performed continuous whisker stimulation; the stimulus had no measurable effect on the probability of an extra spike (paired *t*-test, $P > 0.9$), so we pooled all data. For the combined intracellular–extracellular recording experiments, we used in addition a silicon extracellular multi-site probe (probe type A-1-16-3mm-50-177, Neuronexus Technologies) which was lowered to 1200 μm from the brain surface at an angle of 60°. Neurons were then patched in layer 2/3, 100–300 μm from the probe. Brief current pulses (2.5–10 ms, 1–3 nA) were injected via the patch pipette at 200–400 ms intervals to trigger spikes, and both the intracellular and extracellular signals were recorded. A total of 13,000 stimuli were injected into ten neurons. When the same spike appeared on more than one extracellular recording site, only one spike from one site was selected for analysis.

Full Methods and any associated references are available in the online version of the paper at www.nature.com/nature.

Received 20 January; accepted 15 April 2010.

1. Richmond, B. J., Optican, L. M., Podell, M. & Spitzer, H. Temporal encoding of two-dimensional patterns by single units in primate inferior temporal cortex. I. Response characteristics. *J. Neurophysiol.* **57,** 132–146 (1987).
2. Victor, J. D. & Purpura, K. P. Nature and precision of temporal coding in visual cortex: a metric-space analysis. *J. Neurophysiol.* **76,** 1310–1326 (1996).
3. Tolhurst, D. J., Movshon, J. A. & Dean, A. F. The statistical reliability of signals in single neurons in cat and monkey visual cortex. *Vision Res.* **23,** 775–785 (1983).
4. Abeles, M. *Corticonics: Neural Circuits of the Cerebral Cortex* (Cambridge Univ. Press, 1991).
5. Izhikevich, E. Polychronization: computation with spikes. *Neural Comput.* **18,** 245–282 (2006).
6. Hecht, S., Shlaer, S. & Pirenne, M. Energy, quanta, and vision. *J. Gen. Physiol.* **25,** 819–840 (1942).
7. Binzegger, T., Douglas, R. J. & Martin, K. A. A quantitative map of the circuit of cat primary visual cortex. *J. Neurosci.* **24,** 8441–8453 (2004).
8. Braitenberg, V. & Schüz, A. *Anatomy of the Cortex* (Springer, 1991).
9. Markram, H., Lübke, J., Frotscher, M., Roth, A. & Sakmann, B. Physiology and anatomy of synaptic connections between thick tufted pyramidal neurones in the developing rat neocortex. *J. Physiol. (Lond.)* **500,** 409–440 (1997).
10. Herrmann, A. & Gerstner, W. Noise and the PSTH response to current transients: I. General theory and application to the integrate-and-fire neuron. *J. Comput. Neurosci.* **11,** 135–151 (2001).

11. Richardson, M. Firing-rate response of linear and nonlinear integrate-and-fire neurons to modulated current-based and conductance-based synaptic drive. *Phys. Rev. E* **76,** 021919 (2007).
12. Song, S., Sjöström, P. J., Reigl, M., Nelson, S. & Chklovskii, D. B. Highly nonrandom features of synaptic connectivity in local cortical circuits. *PLoS Biol.* **3,** e68 (2005).
13. Barbour, B., Brunel, N., Hakim, V. & Nadal, J. P. What can we learn from synaptic weight distributions? *Trends Neurosci.* **30,** 622–629 (2007).
14. Thomson, A. M. & Lamy, C. Functional maps of neocortical local circuitry. *Front. Neurosci* **1,** 19–42 (2007).
15. Holmgren, C., Harkany, T., Svennenfors, B. & Zilberter, Y. Pyramidal cell communication within local networks in layer 2/3 of rat neocortex. *J. Physiol. (Lond.)* **551,** 139–153 (2003).
16. Crochet, S. & Petersen, C. C. Correlating whisker behavior with membrane potential in barrel cortex of awake mice. *Nature Neurosci.* **9,** 608–610 (2006).
17. Ferezou, I., Bolea, S. & Petersen, C. C. Visualizing the cortical representation of whisker touch: voltage-sensitive dye imaging in freely moving mice. *Neuron* **50,** 617–629 (2006).
18. Larkum, M. E., Zhu, J. J. & Sakmann, B. A new cellular mechanism for coupling inputs arriving at different cortical layers. *Nature* **398,** 338–341 (1999).
19. Ariav, G., Polsky, A. & Schiller, J. Submillisecond precision of the input-output transformation function mediated by fast sodium dendritic spikes in basal dendrites of CA1 pyramidal neurons. *J. Neurosci.* **23,** 7750–7758 (2003).
20. Häusser, M. & Mel, B. Dendrites: bug or feature? *Curr. Opin. Neurobiol.* **13,** 372–383 (2003).
21. London, M. & Häusser, M. Dendritic computation. *Annu. Rev. Neurosci.* **28,** 503–532 (2005).
22. Murayama, M. *et al.* Dendritic encoding of sensory stimuli controlled by deep cortical interneurons. *Nature* **457,** 1137–1141 (2009).
23. van Vreeswijk, C. & Sompolinsky, H. Chaos in neuronal networks with balanced excitatory and inhibitory activity. *Science* **274,** 1724–1726 (1996).
24. van Vreeswijk, C. & Sompolinsky, H. Chaotic balanced state in a model of cortical circuits. *Neural Comput.* **10,** 1321–1371 (1998).
25. Banerjee, A., Seriès, P. & Pouget, A. Dynamical constraints on using precise spike timing to compute in recurrent cortical networks. *Neural Comput.* **20,** 974–993 (2008).
26. Izhikevich, E. M. & Edelman, G. M. Large-scale model of mammalian thalamocortical systems. *Proc. Natl Acad. Sci. USA* **105,** 3593–3598 (2008).
27. Smale, S. Differentiable dynamical systems. *Bull. Am. Math. Soc.* **73,** 747–817 (1967).
28. Arabzadeh, E., Panzeri, S. & Diamond, M. Deciphering the spike train of a sensory neuron: counts and temporal patterns in the rat whisker pathway. *J. Neurosci.* **26,** 9216–9226 (2006).
29. Bair, W. & Koch, C. Temporal precision of spike trains in extrastriate cortex of the behaving macaque monkey. *Neural Comput.* **8,** 1185–1202 (1996).
30. de Kock, C. P. & Sakmann, B. Spiking in primary somatosensory cortex during natural whisking in awake head-restrained rats is cell-type specific. *Proc. Natl Acad. Sci. USA* **106,** 16446–16450 (2009).

Supplementary Information is linked to the online version of the paper at www.nature.com/nature.

Acknowledgements We thank P. Dayan for discussions, I. van Welie and P. Dayan for comments on the manuscript, and H. Cuntz for comments on the spike detection algorithm. P.E.L. was supported by the Gatsby Charitable Foundation and US National Institute of Mental Health grant R01 MH62447. M.L., A.R., L.B. and M.H. were supported by the Wellcome Trust, the Gatsby Charitable Foundation, the Engineering and Physical Sciences Research Council and the Medical Research Council.

Author Information Reprints and permissions information is available at www.nature.com/reprints. The authors declare no competing financial interests. Readers are welcome to comment on the online version of this article at www.nature.com/nature. Correspondence and requests for materials should be addressed to P.E.L. (pel@gatsby.ucl.ac.uk).

METHODS

Animals and surgery. The care and experimental manipulation of the animals was performed in accordance with institutional and national guidelines. For all experiments, Sprague-Dawley rats (postnatal day 18–25, average 45.6 g) were anaesthetized with urethane (Sigma; 1.5 g kg^{-1}, intraperitoneally). A small craniotomy (1 mm^2) in a region overlying S1 (centred 5.5 mm lateral and 2.5 mm caudal of the bregma) was made and a small opening (~0.1 mm^2) was made in the dura. Supplemental urethane (10% of original dose, intraperitoneally) was given whenever limb withdrawal responses were present or whisker movements were observed. Body temperature was maintained at 37 °C with a feedback-controlled heating blanket.

***In vivo* patch-clamp recording.** For the current injection experiments (summarized in Fig. 3, main text), whole-cell patch-clamp recordings were made using blind patch techniques[31]. Standard borosilicate glass patch pipettes (5.5 MΩ) were filled with internal solution containing the following (in mM): K-methanesulphonate 110, KCl 15, HEPES 10, Mg-ATP 4, Na_2GTP 0.3, Na-phosphocreatine 10, and 0.3% biocytin; pH 7.2, 285 mOsm. Access resistance was typically 20–40 MΩ at the start of the recording and degraded with time. When access resistance rose above 100 MΩ, the recordings were not included in the analysis. Recordings were made at a depth of 1,180 ± 165 μm, and neurons were identified as layer 5 pyramidal cells by input resistance, firing properties and in five cases by cell morphology ($n = 5/5$). Data were filtered at 3–10 kHz and acquired at 50 kHz using Axograph software (Axon Instruments) and an ITC-18 interface (Instrutech). Input resistance was calculated by fitting a linear function to the steady-state current–voltage curve (obtained from voltage deflections during 400-ms current steps from −300 pA to +500 pA in 100-pA steps). EPSC waveforms were generated by a double exponential current injection with $\tau_{rise} = 0.3$ ms and $\tau_{decay} = 1.7$ ms (ref. 32). The experimental protocol consisted of a train of 50 EPSC waveforms separated by 200 ms with alternating amplitudes of either +50, −25, +25, −50 pA or +100, −50, +50, −100 pA. In six of the experiments, diffuse whisker stimulation was delivered by a custom-made motor rotating at 1 Hz driving a 1-cm diameter disk covered with grade 0 sandpaper. The sandpaper touched the primary whisker and the two adjacent whiskers on the same row (all other whiskers were trimmed). The primary whisker was identified before recording by monitoring the local field potential with a low resistance (1 MΩ) electrode filled with artificial cerebrospinal fluid. Stimuli with and without whisker stimulation were interleaved. The stimulus had no measurable effect on the probability of an extra spike (paired *t*-test, $P > 0.9$), so we pooled all data.

***In vivo* simultaneous patch-clamp and extracellular recording.** For the simultaneous patch-clamp and extracellular recordings, a silicon extracellular 16-site linear probe (type A-1-16-3mm-50-177, Neuronexus Technologies) was lowered 1,200 μm from the brain surface at an angle of 60°. After identification of clear spiking units, a patch pipette was inserted and lowered to 250 μm from the brain surface, at a perpendicular distance of 100–300 μm from the probe (calculated based on the distance and the angle between the two electrodes using a custom made system by Luigs & Neumann). We then searched for cells in 2-μm steps. After establishing a whole-cell recording, brief current pulses (2.5–10 ms, 1–3 nA) were injected via the patch pipette into the recorded neuron at 200–400 ms intervals, and both the intracellular and extracellular signals were recorded using an RX5 Pentusa system (Tucker Davis). Ideally, we would have liked to have chosen the amplitude and duration of the current pulses so that each stimulus produced exactly one spike. However, because of up and down states, this was not possible: a stimulus strong enough to always trigger a spike in the down state would be strong enough to regularly produce more than one spike in the up state. Thus we adjusted the strength of the stimulus so that it rarely produced more than one spike. We were largely successful: out of the 13,000 stimuli we delivered (in ten experiments), only 498 (3.8%) produced two spikes. Given the linearity between presynaptic and postsynaptic spikes (Fig. 3b), the small fraction of stimuli that elicited two spikes should have virtually no effect on our results.

Because spikes were far less likely to occur in the down state than the up state, the number of spikes in the intracellularly recorded neuron was correlated with ongoing activity, and thus correlated with spikes on the extracellular electrodes. Thus, to ensure a flat baseline, we constructed PSTHs triggered on stimulus onset, not on intracellular spike times. As can be seen in Fig. 4c, this strategy was successful, as the PSTH was indeed flat before stimulus onset.

The peak in the PSTH after stimulus onset (Fig. 4c) was small, but the fact that 16 consecutive 5-ms bins were more than one standard deviation above the mean suggests that it is significant. To test this, we constructed a cumulative PSTH by subtracting the baseline (the mean firing rate between −100 and 0 ms) from the PSTH and integrating the difference (starting from $t = 0$ and integrating in both directions). To compute error bars, we used a bootstrap method in which we constructed surrogate PSTHs by randomly sampling 200-ms epochs from the extracellular spike trains. We constructed 10,000 surrogate PSTHs, which we turned into cumulative PSTHs as described above. This gave us a null distribution of cumulative PSTHs at each time point; we used those to construct the error bars shown in Fig. 4d.

Spike detection. The extracellular signal was separated online into a local field potential component (0–0.3 kHz) sampled at 3 kHz, and a high frequency component (0.3–5 kHz) sampled at 25 kHz. Spike detection was done offline using the high frequency component of the extracellular signal, as described in Supplementary Information, section 1.

Biophysical models and network simulations. Simulations using a detailed model of a layer 5 pyramidal neuron were based on a published model[33] with slight modifications, and were performed in the NEURON simulation environment[34] (see Supplementary Information, section 4). The network simulations were also based on a previously published model[35], but with modifications to allow the addition and detection of extra spikes (see Supplementary Information, section 7).

31. Margrie, T. W., Brecht, M. & Sakmann, B. In vivo, low-resistance, whole-cell recordings from neurons in the anaesthetized and awake mammalian brain. *Pflügers Arch.* **444,** 491–498 (2002).
32. Häusser, M. & Roth, A. Estimating the time course of the excitatory synaptic conductance in neocortical pyramidal cells using a novel voltage jump method. *J. Neurosci.* **17,** 7606–7625 (1997).
33. Mainen, Z. F., Joerges, J., Huguenard, J. R. & Sejnowski, T. J. A model of spike initiation in neocortical pyramidal neurons. *Neuron* **15,** 1427–1439 (1995).
34. Hines, M. L. & Carnevale, N. T. The NEURON simulation environment. *Neural Comput.* **9,** 1179–1209 (1997).
35. Latham, P. E., Richmond, B. J., Nelson, P. G. & Nirenberg, S. N. Intrinsic dynamics in neuronal networks: I. Theory. *J. Neurophysiol.* **83,** 808–827 (2000).